



ISTITUTO NAZIONALE DI RICERCA METROLOGICA Repository Istituzionale

In silico evaluation of adverse eddy current effects in preclinical tests of magnetic hyperthermia

This is the author's accepted version of the contribution published as:

Original

In silico evaluation of adverse eddy current effects in preclinical tests of magnetic hyperthermia / Vicentini, Marta; Vassallo, Marta; Ferrero, Riccardo; Androulakis, Ioannis; Manzin, Alessandra. - In: COMPUTER METHODS AND PROGRAMS IN BIOMEDICINE. - ISSN 0169-2607. - 223:(2022), p. 106975. [10.1016/j.cmpb.2022.106975]

Availability:

This version is available at: 11696/76260 since: 2023-07-06T16:10:17Z

Publisher:

ELSEVIER IRELAND LTD

Published

DOI:10.1016/j.cmpb.2022.106975

Terms of use:

This article is made available under terms and conditions as specified in the corresponding bibliographic description in the repository

Publisher copyright

(Article begins on next page)

***In silico* evaluation of adverse eddy current effects in preclinical tests of magnetic hyperthermia**

Marta Vicentini^{a,b}, Marta Vassallo^{a,b}, Riccardo Ferrero^a, Ioannis Androulakis^c, Alessandra Manzin^a

^a*Istituto Nazionale di Ricerca Metrologica (INRIM), Strada delle Cacce 91, 10135 Torino, Italy*

^b*Politecnico di Torino, Corso Duca degli Abruzzi 24, 10129 Torino, Italy*

^c*Erasmus MC Cancer Institute, University Medical Center, 3015 GD Rotterdam, The Netherlands*

Corresponding authors:

Marta Vicentini

Istituto Nazionale di Ricerca Metrologica

Strada delle Cacce 91

10135 Torino, Italy

tel. +39-011-3919830

e-mail: m.vicentini@inrim.it

Alessandra Manzin

Istituto Nazionale di Ricerca Metrologica

Strada delle Cacce 91

10135 Torino, Italy

tel. +39-011-3919825

e-mail: a.manzin@inrim.it

Abstract

Background and Objective: Magnetic hyperthermia is an oncological therapy that employs magnetic nanoparticles activated by alternating current (AC) magnetic fields with frequencies between 50 kHz and 1 MHz, to release heat in a diseased tissue and produce a local temperature increase of about 5 °C. To assess the treatment efficacy, *in vivo* tests on murine models (mice and rats) are typically performed. However, these are often carried out without satisfying the biophysical constraints on the electromagnetic (EM) field exposure, with consequent generation of hot spots and undesirable heating of healthy tissues. Here, we investigate possible adverse eddy current effects, to estimate AC magnetic field parameters (frequency and amplitude) that can potentially guarantee safe animal tests of magnetic hyperthermia. **Methods:** The analysis is performed through *in silico* modelling by means of finite element simulation tools, specifically developed to study eddy current effects in computational animal models, during magnetic hyperthermia treatments. The numerical tools enable us to locally evaluate the specific absorption rate (SAR) and the produced temperature increase, under different field exposure conditions. **Results:** The simulation outcomes demonstrate that in mice with weight lower than 30 g the thermal effects induced by AC magnetic fields are very weak, also when slightly overcoming the Hergt-Dutz limit, that is the product of the magnetic field amplitude and frequency should be lower than $5 \cdot 10^9$ A/(m·s). Conversely, we observe significant temperature increases in 500 g rats, amplified when the field is applied transversally to the body longitudinal axis. A strong mitigation of side-effects can be achieved by introducing water boluses or by applying focused fields. **Conclusions:** The developed physics-based modelling approach has proved to be a useful predictive tool for the optimization of preclinical tests of magnetic hyperthermia, allowing the identification of proper EM field conditions and the design of setups that guarantee safe levels of field exposure during animal treatments. In such context, the obtained results can be considered as valid indicators to assess reference levels for animal testing of biomedical techniques that involve EM fields, like magnetic hyperthermia, thus complying with the Directive 2010/63/EU on the protection of animals used for scientific purposes.

Keywords: Bio-heat transfer model; Magnetic hyperthermia; Magnetic nanoparticles; Magnetic field applicators; Numerical simulations; Specific absorption rate; *In silico* modelling; Computational animal models; Preclinical tests.

1. Introduction

Hyperthermia is a non-conventional therapy for cancer treatment, which consists in the generation of high temperatures in a tumour-affected region, within the range 39-45 °C [1,2]. This medical technique has been shown to provide benefits in oncology due to its tumour selectivity and minimal injury to normal tissues: a rise in temperature promotes irreversible damage of cancer cells, more susceptible to heat than healthy ones for their reduced oxygenation [3]. A great contribution of hyperthermia to cancer treatment is the ability to enhance the effectiveness of other therapies, like radiotherapy and chemotherapy [2-4].

Among the different ways of delivering heat in diseased tissues, magnetic hyperthermia has gained a lot of attention, due to its ability to induce a localized increase in temperature with reduced side-effects [5-8]. This is achieved by means of magnetic nanoparticles (MNPs) excited by alternating current (AC) magnetic fields with frequency between 50 kHz and 1 MHz [9]. For safety reasons, it is necessary to impose restrictions on the product of the peak amplitude (\hat{H}_a) and frequency (f) of the AC magnetic field. In fact, the exposure to magnetic fields with large amplitude and/or frequency can lead to the occurrence of hot spots even in healthy tissues, as a consequence of eddy current heating [10]. To reduce health risks as much as possible, a biophysical constraint on the AC magnetic field parameters was proposed in 1984, known as the Atkinson-Brezovich limit, that is $\hat{H}_a \times f \leq 4.85 \cdot 10^8 \text{ A/(m}\cdot\text{s)}$ [11]; subsequently, a less rigid limit, $\hat{H}_a \times f \leq 5 \cdot 10^9 \text{ A/(m}\cdot\text{s)}$, was introduced by Hergt and Dutz [12].

Despite the above indications, several preclinical studies (i.e. *in vivo* tests on animals) have been performed without satisfying the safety criteria suggested for magnetic hyperthermia. In many tests conducted on murine models (mice and rats), the AC magnetic field parameters have been selected without fulfilling even the less rigid limit of Hergt-Dutz [13-26], to exploit as much as possible the MNP heating capabilities. This fact, which is well documented in recent reviews [27,28], poses severe questions on the animal welfare during and after the experiments, and on the possibility to translate to humans the outcomes obtained in tests on animals. Moreover, it makes complex a correct estimation of the real MNP heating efficiency in tissues, due to the difficulties in distinguishing the heating contribution of MNPs from the one of the radiofrequency electromagnetic (EM) field alone, which cannot be negligible for large values of \hat{H}_a or f .

Information about the effects on animals of the exposure to radiofrequency EM fields can be found in the guidelines released by the International Commission on Non-Ionizing Radiation Protection (ICNIRP), which

are not conceived for medical purposes, but to provide safe levels for EM field human exposure in occupational and general public scenarios. In particular, ICNIRP provided reference levels for the whole-body average specific absorption rate (SAR), which indicates the power absorbed, per unit of mass, averaged over the entire body [29]. In animals, harm was only found under conditions of exposure characterized by a whole-body average SAR substantially higher than 4 W/kg; this value can be assumed as the threshold below which adverse effects would not be expected [30]. In the ICNIRP guidelines, the results on animals were reported as an additional proof to extrapolate safe limits of EM field exposure for humans, but from a research point of view can be also considered as indicators for performing safe preclinical tests of biomedical techniques that involve EM fields, like magnetic hyperthermia. In particular, such outcomes can guide the selection of magnetic field parameters that enable to reduce unnecessary pain for the animals, also in compliance with the Directive 2010/63/EU of the European Parliament on the protection of animals used for scientific purposes.

Another critical aspect in preclinical studies is the design of the magnetic field sources, which have to generate a field in the target region sufficiently uniform and large to activate the MNPs, whose specific loss power is an increasing function of both field amplitude and frequency [31,32]. At the moment, there are no standards for the setups used *in vivo*. Although some commercial applicators are specifically manufactured for preclinical experiments on mice [33], many research groups build their own applicators to better adapt them to the size of animals and tumours to be treated. Different coil geometries and experimental settings were proposed, comprising helical or Helmholtz coils with animals placed totally or partially inside [34,35], and helical or pancake coils not surrounding the animal body, but positioned close to the tumour site [36,37]. However, not always the biophysical constraints on the AC magnetic field [11,12] are satisfied [13-26].

In this paper, we perform *in silico* experiments on high-resolution digital phantoms of two murine models (a 30 g mouse and a 500 g rat) to investigate the effects of the only EM field exposure in magnetic hyperthermia preclinical tests. The aim is to provide indications to avoid as much as possible eddy current generation and appearance of undesirable hot spots, which can cause discomfort and tissue damage to the animals. First, we evaluate the SAR and temperature increase under the application of uniform AC magnetic fields with variable frequency and peak amplitude. In this case, we also analyse the role of magnetic field direction (parallel or perpendicular to the body longitudinal axis), body size and type of heat exchange between the skin and the environment. Particular attention is paid to the conditions overcoming the Hergt-Dutz limit. Second, we

compare two different kinds of local magnetic field applicators already used in preclinical tests, namely a helical coil and a pancake coil. In particular, we investigate the eddy current mitigation consequent to a more focused EM field exposure, by evaluating SAR and temperature increase in the exposed tissues as a function of the applicator geometry.

The study is performed by means of in-house finite element models. The eddy current effects produced in the biological tissues during the AC magnetic field application are evaluated with a low-frequency EM field solver, in which displacement currents are neglected. The induced thermal effects are calculated with a numerical code that solves the Pennes' bio-heat transfer equation.

2. Methods

The analysis is performed by means of in-house numerical models aimed at determining SAR and thermal effects correlated to the exposure to the only AC magnetic field. The numerical solutions are obtained by using the finite element method (FEM) with linear shape functions, after discretizing the 3D domain under analysis Ω_b into tetrahedral elements. In the following, Ω_b represents the region occupied by the animal body (with boundary $\partial\Omega_b$).

2.1 Simulation of eddy current effects

A low-frequency EM field solver is developed to calculate the eddy current effects produced in biological tissues during AC magnetic field application. Within the frequency range of interest for magnetic hyperthermia (50 kHz – 1 MHz), the EM field wavelength is much larger than the size of Ω_b , thus we can consider a quasi-static approximation, neglecting displacement currents. Due to the low electrical conductivity (σ) of tissues, we can assume that the magnetic field is not modified in an appreciable way by the induced eddy currents. Hence, the electric field vector \mathbf{E} inside Ω_b is expressed as

$$\mathbf{E} = -\nabla\phi - j\omega\mathbf{A}_s, \quad (1)$$

where ω is the angular frequency, j is the imaginary unit, ϕ is the electric scalar potential and \mathbf{A}_s is the magnetic vector potential due to the magnetic field sources [38]. The introduction of the charge conservation equation leads to

$$\nabla \cdot (\sigma \nabla \phi) = -j\omega \nabla \cdot (\sigma \mathbf{A}_s), \quad (2)$$

combined to the following boundary condition on $\partial\Omega_b$ (with \mathbf{n} being the normal unit vector):

$$\frac{\partial \phi}{\partial n} = -j\omega \mathbf{A}_s \cdot \mathbf{n}. \quad (3)$$

The unknown ϕ is obtained by FEM, applied to the weak formulation of (2) with linear basis function w , namely:

$$\int_{\Omega_b} \sigma \nabla \phi \cdot \nabla w dv_b = -j\omega \int_{\Omega_b} \sigma \mathbf{A}_s \cdot \nabla w dv_b. \quad (4)$$

After solving (4) the whole-body average SAR is calculated as

$$\text{SAR} = \frac{1}{V_b} \int_{\Omega_b} \frac{\sigma |E|^2}{2\rho} dv_b, \quad (5)$$

where V_b is the body volume and ρ is the tissue density.

In presence of source conductors with complex geometry, the magnetic vector potential \mathbf{A}_s in (4) is computed numerically, as:

$$\mathbf{A}_s(\mathbf{r}_b) = \frac{\mu_0}{4\pi} \int_{\Omega_s} \frac{\mathbf{J}_s(\mathbf{r}_s)}{|\mathbf{r}_b - \mathbf{r}_s|} dv_s, \quad (6)$$

where μ_0 is the vacuum magnetic permeability, \mathbf{J}_s is the current density vector in a point with vector position \mathbf{r}_s inside the source conductors (3D domain Ω_s) and \mathbf{r}_b is the vector position of a point in Ω_b . The spatial distribution of \mathbf{J}_s within Ω_s is calculated by solving the current-field equation with FEM under quasi-static conditions, considering current driven formulation [39]. Once known \mathbf{J}_s , we can evaluate \mathbf{A}_s for determining \mathbf{E} and the magnetic field in the body, as:

$$\mathbf{H}_s(\mathbf{r}_b) = \frac{1}{4\pi} \int_{\Omega_s} \frac{\mathbf{J}_s(\mathbf{r}_s) \times (\mathbf{r}_b - \mathbf{r}_s)}{|\mathbf{r}_b - \mathbf{r}_s|^3} dv_s. \quad (7)$$

2.2 Simulation of thermal effects

To calculate the thermal effects induced in the animal body Ω_b due to the exposure to the AC magnetic field, we implement a FEM code that solves the Pennes' bio-heat transfer equation [40]

$$\rho C_p \frac{\partial T}{\partial t} = \nabla \cdot k \nabla T + Q_m - WC_{\text{blood}}(T - T_{\text{blood}}) + Q_s, \quad (8)$$

In (8) T is the local tissue temperature, C_p is the tissue heat capacity, k is the tissue thermal conductivity, Q_m is the metabolic heat generation rate per unit volume, W is the local tissue-blood perfusion rate, C_{blood} is the heat capacity of blood and T_{blood} is the arterial temperature [41]. C_{blood} and T_{blood} are fixed to 3617 J/(K·kg) and 37 °C, respectively. The external power deposition term is Q_s , which is the heating power produced by the AC magnetic field per unit volume; here, the heat released by the MNPs is not included.

Equation (8) is completed by the following boundary condition at the interface $\partial\Omega_b$ between the skin and the surrounding environment:

$$q = -k \frac{\partial T}{\partial n} = -h(T_{\text{ext}} - T_{\text{skin}}), \quad (9)$$

where q is the outward heat flux, T_{ext} is the external temperature (set at 25 °C), T_{skin} is the skin temperature and h is the heat transfer coefficient.

At $t = 0$, $T = T_0$, which corresponds to the baseline temperature or steady-state temperature before heating, governed by the metabolic heat.

The application of the weak formulation to (8) leads to:

$$\begin{aligned} \int_{\Omega_b} \rho C_p \frac{\partial T}{\partial t} w dv_b + \int_{\Omega_b} k \nabla T \cdot \nabla w dv_b + \int_{\Omega_b} WC_{\text{blood}} T w dv_b + \int_{\partial\Omega_b} h T_{\text{skin}} w ds_b = \\ \int_{\partial\Omega_b} h T_{\text{ext}} w ds_b + \int_{\Omega_b} WC_{\text{blood}} T_{\text{blood}} w dv_b + \int_{\Omega_b} Q_m w dv_b + \int_{\Omega_b} Q_s w dv_b \end{aligned}, \quad (10)$$

The time integration of (10) is performed with the Crank-Nicholson's method [42].

Thermoregulation or temperature-dependence of blood perfusion phenomena is also considered following the approach described in [43]. This consists in multiplying the blood perfusion term in (8) by a local temperature-dependent coefficient L_{blood} , defined as:

$$L_{\text{blood}} = 2 \frac{T - T_0}{\Delta B}, \quad (11)$$

where ΔB is the local vasodilation parameter, here assumed equal to 4 K or 10 K. According to [43], coefficient L_{blood} is limited to 15 for all tissues except for skin, where the limit is set at 32. The non-linearity introduced in the modified version of (8) is handled with an iterative method.

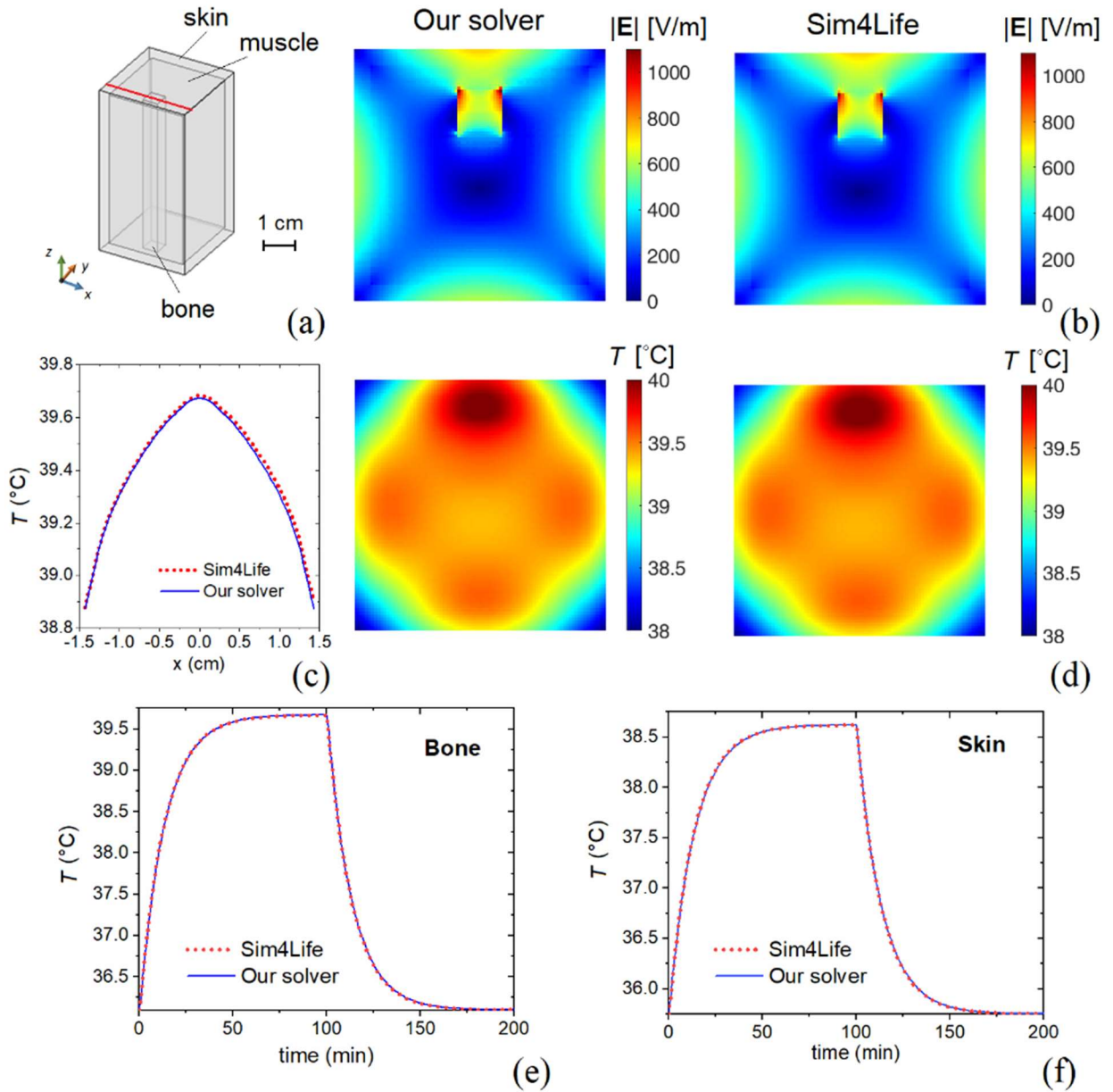


Fig. 1. (a) Schematic of the sample considered for numerical model validation. (b) Comparison of the maps of the electric field amplitude, calculated on the median cross-section with our solver (left) and Sim4Life (right). (c) Spatial variation of the temperature at equilibrium, calculated along the red line depicted in the schematic in (a). (d) Comparison of the maps of the temperature at equilibrium, calculated on the median cross-section with our solver (left) and Sim4Life (right). Comparison of the time evolutions of the temperature calculated in two different points, located in (e) bone region and (f) skin region.

3. Method Validation

The developed EM and thermal solvers are validated by comparison to the numerical models implemented in the computation platform Sim4Life (v6.2, ZMT, Zurich, Switzerland), using the structured-grid FEM solver for the EM problem and the finite-difference time-domain (FDTD) method for the thermal problem [44]. The results are obtained on a simplified geometry, schematized in Fig. 1a, consisting in a rectangular prism with size of $2.9 \times 2.9 \times 5.4 \text{ cm}^3$ and composed of three regions of different materials, namely:

- an outer 2 mm thick layer with skin properties, i.e. $\sigma = 0.17 \text{ S/m}$, $\rho = 1109 \text{ kg/m}^3$, $k = 0.372 \text{ W/(K}\cdot\text{m)}$, $C_p = 3390.5 \text{ J/(K}\cdot\text{kg)}$, $Q_m = 1827.1 \text{ W/m}^3$ and $W = 2.203 \text{ kg/(s}\cdot\text{m}^3)$;
- an internal rectangular prism with $5 \times 5 \text{ mm}^2$ cross-section and bone properties, i.e. $\sigma = 0.0035 \text{ S/m}$, $\rho = 1908 \text{ kg/m}^3$, $k = 0.32 \text{ W/(K}\cdot\text{m)}$, $C_p = 1312.8 \text{ J/(K}\cdot\text{kg)}$, $Q_m = 295.5 \text{ W/m}^3$ and $W = 0.356 \text{ kg/(s}\cdot\text{m}^3)$;
- the remaining volume with muscle properties, i.e. $\sigma = 0.355 \text{ S/m}$, $\rho = 1090.4 \text{ kg/m}^3$, $k = 0.495 \text{ W/(K}\cdot\text{m)}$, $C_p = 3421.2 \text{ J/(K}\cdot\text{kg)}$, $Q_m = 988 \text{ W/m}^3$ and $W = 0.748 \text{ kg/(s}\cdot\text{m}^3)$.

The heat transfer coefficient h on the external surfaces is set at $3.5 \text{ W/(m}^2\cdot\text{K)}$. The simulations are performed considering a uniform mesh grid with 0.6 mm size.

First, we test the low-frequency EM field solver, considering as external source an AC magnetic field uniformly applied along the longitudinal axis, with a frequency of 100 kHz and a peak amplitude of 80 kA/m. Fig. 1b compares the maps of the electric field amplitude, calculated on the median cross-section with our solver and Sim4Life; the results are in good agreement, with an average discrepancy of 1.2%, associated with an average discrepancy on local SAR of 2.3%.

Second, we test the thermal solver in the stationary case, considering as an input the heating power per unit volume, i.e. Q_s in (8), previously determined with the low-frequency EM field solvers. Fig. 1c and Fig. 1d compare the spatial distributions of the temperature at equilibrium, calculated respectively along a line parallel to x -axis intersecting the bone region and on the median cross-section; the results obtained with our solver and Sim4Life are in very good agreement, with an average discrepancy of 0.008%.

Third, we test the thermal solver in the transient case, simulating a heating process with a duration of 100 min, followed by a cooling process with a duration of 100 min; for both our solver and Sim4Life the time-step is fixed to 1 min. For the initial condition we consider the temperature spatial distribution evaluated in the

absence of the EM field; the heating process is driven by the same spatial distributions of Q_s inputted in the stationary cases. The results are compared in Fig. 1e and Fig. 1f, which show the time evolutions of the temperature calculated in two different points, one located in the bone region (Fig. 1e) and the other one in the skin region (Fig. 1f). The discrepancies averaged over the entire time interval are in the order of 0.02%, confirming the good agreement between our solver and Sim4Life also for the transient case.

4. Results and Discussion

In this section we elucidate the role of magnetic field sources on the safety of magnetic hyperthermia preclinical tests. To this aim, we mimic the *in vivo* experiments by means of *in silico* simulations performed on high-resolution digital phantoms of two murine models with realistic geometry and tissue properties. The detailed anatomical structures of the two voxel-based phantoms, which are provided by IT'IS Foundation under license [45], were generated from magnetic resonance, x-ray CT or cryosection image data [46]. The considered murine models have very different size; the smaller one is a male nude normal mouse with a length of 8.6 cm (excluding tail) and a weight of 28 g; the bigger one is a Sprague Dawley rat with a length of 22.5 cm (excluding tail) and a weight of 503 g, with three tumours located in the bottom part of the body. The mouse and rat models are resampled to isotropic 0.25 mm and 1 mm voxel size, respectively.

The electrical conductivity, density and thermal properties of the tissues are extracted from the IT'IS Foundation database [47], except for the properties of the tumours within the Sprague Dawley rat. In this case, σ is set at 0.8 S/m [48], ρ at 1045 kg/m³, C_p at 3760 J/(K·kg), k at 0.51 W/(K·m), Q_m at 31872.5 W/m³ and W at 9.97 kg/(s·m³) [41].

We analyse the role on eddy current heating of the following parameters: peak amplitude \hat{H}_a and frequency f of the AC magnetic field; animal body size; orientation of the field with respect to the body (under the assumption of field uniformity); applicator geometry (case of non-uniform field). The impact of these parameters can be deduced from the following approximated expression for the specific heating power produced by eddy currents in a cylindrical uniform sample

$$P = \sigma (\pi \mu_0)^2 (\hat{H}_a f)^2 r^2, \quad (12)$$

where r is the radial distance from the cylinder axis [11].

To evaluate the role on thermal response of forced thermal convection (e.g. presence of a water bolus), we also consider different values of the heat transfer coefficient h at the skin interface with the surrounding environment. If not directly specified, this is assumed equal to $3.5 \text{ W}/(\text{m}^2 \cdot \text{K})$ [48], to simulate a condition where free convection prevails.

4.1 Influence of magnetic field amplitude and frequency

Many preclinical tests of magnetic hyperthermia have been conducted without fulfilling the biophysical limits on the exposure to radiofrequency EM fields [27,28]. In particular, in almost all the investigations on murine models the Atkinson-Brezovich limit was not satisfied, considering only the restrictions imposed by Hergt-Dutz, e.g. in [49-53]. As listed in Table 1, there are also studies in which even the less rigid criterion of Hergt-Dutz was exceeded; these were mainly performed on mice with a weight lower than 30 g [13-25]. Anyway, in [26] 250-270 g rats were exposed to a field with an amplitude of 14 kA/m and a frequency of 606 kHz, corresponding to a product $\dot{H}_a \times f$ of $8.5 \cdot 10^9 \text{ A}/(\text{m} \cdot \text{s})$.

A non-careful selection of the AC magnetic field parameters may lead to non-negligible eddy current heating, thus impacting on the animal welfare as well as on the correct evaluation of the MNP heating efficiency. During *in vivo* treatments the thermal dose is indeed a result of the heating induced by the MNP activation as well as by the possible eddy current effects arising when applying AC magnetic fields with large amplitude and/or frequency. The simultaneous presence of the two phenomena makes critical the experimental quantification of the two contributions, as outlined in [54], which proposed a methodology that is a step forward towards the *in vivo* estimation of the SLP of MNPs as well as of the SAR from EM field exposure.

In order to check the safety of preclinical tests in terms of EM dosimetry, we investigate the influence of the field peak amplitude \dot{H}_a and frequency f on the induced eddy current heating. The analysis is initially focused on the 28 g mouse, which is one of the most typical murine models used in preclinical tests. The field is first assumed to be uniformly distributed along the body longitudinal axis, hypothesis that can be considered acceptable when the animal is placed totally within a helical coil or solenoid.

Table 1
Data from preclinical studies of magnetic hyperthermia exceeding the Hergt-Dutz limit

Ref.	Animal model	Tumour size and location	Applicator and exposure type	\dot{H}_a [kA/m]	f [kHz]	$\dot{H}_a \times f$ [A/(m·s)]	Heating time [min]
[13]	Athymic nude mouse	100-250 mm ³ (backside area)	Helical coil (backside external exposure)	15.4	435	$6.7 \cdot 10^9$	60 (more cycles)
[14]	Athymic nude mouse	200 mm ³ (backside area)	Helical coil (backside external exposure)	15.4	435	$6.7 \cdot 10^9$	60
[15]	Athymic nude mouse (~30 g)	200 mm ³ (flank area)	Helmholtz coil (body inside)	14.3	470	$6.7 \cdot 10^9$	5 (more cycles)
[16]	Athymic nude mouse (~30 g)	500 mm ³ (flank area)	Helmholtz coil (body inside)	14.3	470	$6.7 \cdot 10^9$	30
[17]	Athymic nude mouse (~20 g)	125 mm ³ (flank area)	Helmholtz coil (body inside)	14.3	470	$6.7 \cdot 10^9$	30
[18]	BALB/c nude mouse (~29-32 g)	100-150 mm ³ (flank area)	Helical coil (body inside)	19.5	389	$7.6 \cdot 10^9$	25 (more cycles)
[19]	HSP70-LucF transgenic mouse (~20 g)	N/A (back area)	Helical coil (body inside)	10.2	755	$7.7 \cdot 10^9$	10
[20]	Mouse	21-30 mm ³ (femoral area)	Helical coil (body inside)	9.3	880	$8.2 \cdot 10^9$	30 (more cycles)
[21]	C3H/HeJ mouse	220±40 mm ³ (breast)	Helical coil (body inside)	55.7	150	$8.4 \cdot 10^9$	15
[22]	BALB/c nude mouse (~18 g)	60 mm ³ (breast)	Helical coil (body inside)	23.9	350	$8.4 \cdot 10^9$	8
[23]	Nude mouse (~26 g)	50 mm ³ (flank area)	Helical coil (posterior half inside)	26.9	420	$11.3 \cdot 10^9$	30 (more cycles)
[24]	SCID Mouse (~18-19 g)	200 mm ³ (flank area)	N/A	31.8	366	$11.6 \cdot 10^9$	10
[25]	BALB/c nude mouse (~20 g)	100 mm ³ (abdomen)	Helical coil (body inside)	37.3	500	$18.7 \cdot 10^9$	10
[26]	Rat (~250-270 g)	460 (±190) mm ³ (liver)	Helical coil (body inside)	14	606	$8.5 \cdot 10^9$	>21

The diagram in Fig. 2 reports the values of the whole-body average SAR calculated by varying \dot{H}_a between 5 kA/m and 75 kA/m and f between 50 kHz and 1 MHz. The markers refer to specific combinations of \dot{H}_a and f from Table 1, for which the maximum temperature increases in the body are also indicated. These are calculated as the maximum differences between the temperature reached at the thermal equilibrium and the initial temperature before field application.

The results reported in Fig. 2 demonstrate that under the Hergt-Dutz limit the whole-body average SAR in mice does not exceed the value of 1 W/kg, whereas the threshold of 4 W/kg is reached when the product $\dot{H}_a \times f$ is $\sim 12 \cdot 10^9$ A/(m·s), which is more than twice the value corresponding to the Hergt-Dutz limit. When this is barely overcome the estimated maximum temperature increase is very low (less than 0.3 °C), but it reaches

values in the order of 0.8 °C in proximity to the SAR threshold of 4 W/kg. When this threshold is largely exceeded, the temperature increase is no more negligible and, according to the ICNIRP guidelines, discomfort to the animals can occur [30]. As an example, when $\hat{H}_a = 37.3$ kA/m and $f = 500$ kHz [25], a maximum temperature increase higher than 2 °C is found on the skin, in correspondence of the lower part of the mouse back. This value is reached in about 50 min of heating and a time interval of 40 min is needed to re-establish the initial temperature, once the field is turned off. If we consider a heating time of 10 min as in [25], the estimated maximum temperature increase is in the order of 2 °C anyway.

For the cases referenced in Fig. 2, the values of the peak spatial SAR averaged over 5 mg of tissue mass [55] vary from 5.9 W/kg, for case $\hat{H}_a \times f = 6.7 \cdot 10^9$ A/(m·s), $\Delta T_{\max} = 0.28$ °C, to 46 W/kg, for case $\hat{H}_a \times f = 18.7 \cdot 10^9$ A/(m·s), $\Delta T_{\max} = 2.16$ °C.

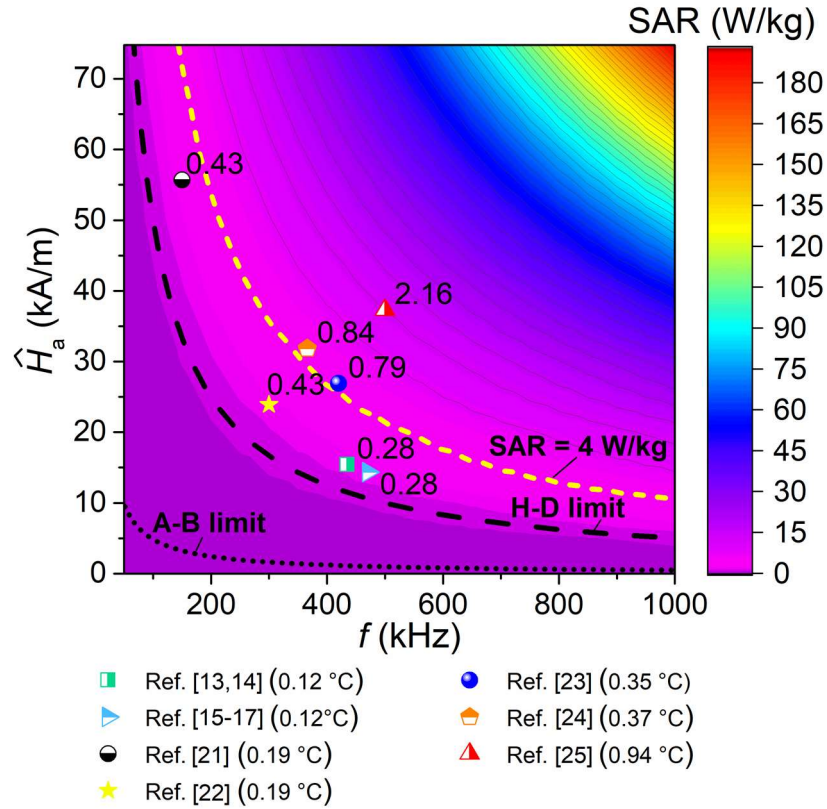


Fig. 2. Whole-body average SAR evaluated for the 28 g mouse, versus magnetic field frequency and amplitude, when the field is uniformly applied along the body longitudinal axis. The values specified beside the markers refer to the maximum temperature increases (in °C), calculated for field parameters used in preclinical tests. The legend reports the relative references, together with the estimated average temperature increases (within the brackets).

4.2 Influence of animal size

The moderate temperature increase observed in mice when exposed to EM fields during magnetic hyperthermia sessions enable us to perform *in vivo* tests of MNPs that require high magnetic fields to be

activated, e.g. disk- or ring-shaped MNPs [56,57]. However, as clearly demonstrated by (12), a significant temperature rise can be obtained if the experiments are performed under the same field conditions on animals with larger size, like rats, as a consequence of the enlargement of the body transversal section [26]. This is depicted in Fig. 3a, which reports the whole-body average SAR, and the maximum and average temperature increases calculated for the 503 g rat, versus $\hat{H}_a \times f$. Also in this case the field is assumed to be uniform and applied along the body longitudinal axis.

Even below the Hertz-Dutzy limit, non-negligible temperature changes can be observed. As an example, when $\hat{H}_a \times f = 4 \cdot 10^9 \text{ A/(m}\cdot\text{s)}$, an average temperature increase of 1.6 °C is reached, with a maximum in the order of 4.6 °C (the corresponding whole-body average SAR and peak spatial SAR averaged over 50 mg of

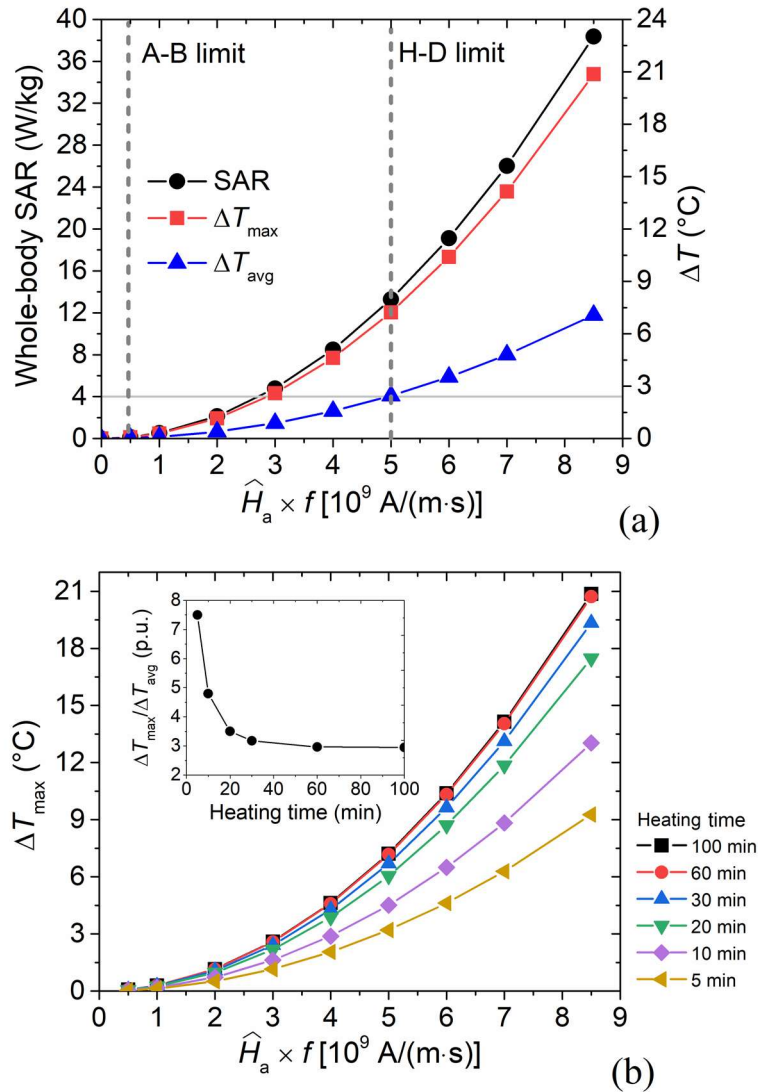


Fig. 3. (a) Whole-body average SAR (left), and maximum and average temperature increases (right) estimated for the 503 g rat, versus the product of the AC magnetic field frequency and peak amplitude. The field is uniformly applied along the body longitudinal axis. (b) Corresponding maximum temperature increase, as a function of heating time (the inset reports the ratio of the maximum to the average temperature increases).

tissue mass [55] are 8.5 W/kg and 37 W/kg, respectively). Maximum temperature increments lower than 1 °C are found only when the product $\hat{H}_a \times f$ does not exceed the value of $2 \cdot 10^9$ A/(m·s) and the whole-body average SAR is lower than 2 W/kg. In correspondence of the Atkinson-Brezovich limit, a negligible increase in temperature is estimated (maximum lower than 0.1 °C), thus not affecting physiological conditions. The obtained results are in line with the experimental findings in [26], where the application of a magnetic field with $\hat{H}_a = 14$ kA/m and $f = 606$ kHz is responsible for a temperature increase around 2 °C in 250-270 g rats.

The heating effects due to the EM field exposure can be mitigated by reducing the time duration of the field application. Anyway, as shown in Fig. 3b, a significant weakening of eddy current effects can be obtained only for very short heating time intervals (e.g. 5-10 min). When the magnetic field is applied for 5 min and $\hat{H}_a \times f = 4 \cdot 10^9$ A/(m·s), the average temperature increase is 0.6 °C, with a maximum of 2.1 °C. It's worth noting that the increase in the heating time leads to an extension of the regions characterized by the highest temperature, i.e. the ratio of the maximum to the average temperature increases reduces from 7.5 to 3, when raising the heating time from 5 min to 60 min (inset of Fig. 3b).

For the rat, the temperature peaks are localized in the regions closest to the skin, especially in correspondence of the hips, where the body is wider. For the mouse the temperature increase is practically negligible. This is well illustrated by Fig. 4a, which compares the spatial distributions of the temperature at the end of the heating transient, calculated over longitudinal sections of the rat and mouse, when $\hat{H}_a = 50$ kA/m and $f = 100$ kHz (Hergt-Dutz limit).

Fig. 4b reports the corresponding time evolutions of the average and maximum temperature increases estimated in the two animals during the heating-cooling transients. The heating phase has a duration (100 min) sufficiently long to ensure the reaching of thermal equilibrium. In the rat an average temperature increase of 2.4 °C is found, associated with a maximum of 7.2 °C, a whole-body average SAR of 13.3 W/kg and a peak spatial SAR averaged over 50 mg of tissue mass of 58 W/kg; whereas the mouse is subjected to very low temperature increments, maintaining the temperature practically stable during all the heating time. It presents an average temperature increase of 0.07 °C, corresponding to a maximum of 0.16 °C and a whole-body average SAR of 0.9 W/kg. Once the field is switched off, the rat needs about 80 min to re-establish the initial temperature, while the mouse 50 min.

It is important to notice that the above results are obtained disregarding thermoregulatory response, i.e.

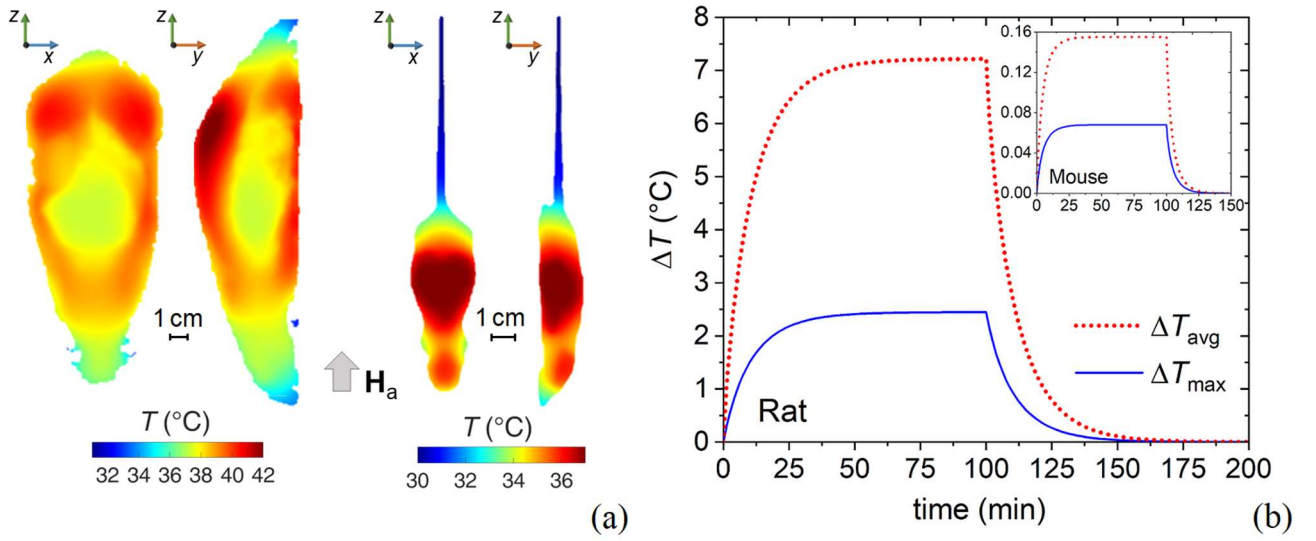


Fig. 4. (a) Maps of the temperature spatial distribution at thermal equilibrium calculated over two longitudinal sections of the 503 g rat (left) and 28 g mouse (right), when the AC magnetic field is applied uniformly along the body longitudinal axis with a peak amplitude of 50 kA/m and a frequency of 100 kHz. (b) Corresponding time evolutions of the average and maximum temperature increases during the heating-cooling transients; the data for the mouse are reported in the inset (with the same measure units of the main graph).

neglecting the dependence of blood perfusion on temperature. This choice is motivated by the fact that, during hyperthermia tests, the animals are generally anesthetized, with the consequent inactivation of thermoregulatory response, accompanied by a reduction in blood flow and basal metabolism [58, 59]. Under these conditions, the eddy current effects are more intense, with major probability of tissue damage. If thermoregulatory mechanisms are present (no anaesthesia is administered), a lower increase in temperature is indeed expected. In particular, the introduction of temperature-dependence of blood perfusion leads to a reduction in the temperature increase in the order of 27% and 15%, when the local vasodilation parameter ΔB in (11) is set at 4 K and 10 K, respectively.

4.3 Influence of magnetic field orientation

In most cases, magnetic hyperthermia preclinical tests are performed by placing the animal body within a helical coil, positioning the tumour at the centre, where the field is higher and more uniform. Typically, the animal longitudinal axis is orientated along the coil vertical axis, but it can be also positioned transversally [60], if the coil is sufficiently large. In this case, as explained by (12), more intense eddy current effects are expected, due to the enlargement of the body section orthogonal to the field.

The results obtained when a uniform field is applied transversally to the animal longitudinal axis are shown in Fig. 5, considering again $\hat{H}_a = 50$ kA/m and $f = 100$ kHz. Under this condition, at thermal equilibrium the

rat experiences an average temperature increase of 4 °C, associated with a maximum of 14.1 °C, a whole-body average SAR of 21.2 W/kg and a peak spatial SAR averaged over 50 mg of tissue mass of 132 W/kg; whereas, in the mouse negligible temperature variations are found (average of 0.11 °C, maximum of 0.31 °C and whole-body SAR of 1.24 W/kg).

The role of the body orientation with respect to the field is clearly deducible from the comparison of Fig. 4a and Fig. 5a. The latter displays the spatial distributions of the temperature at the end of the heating transient, calculated over longitudinal sections of the rat and mouse, when the field is applied transversally to the body vertical axis. The mouse presents a temperature map that is not significantly affected by the field orientation, due to the negligible influence of the field itself. The temperature spatial distribution is similar to the one observed when the field is absent, that is, the tail as the coldest part, and the abdomen and the head as the warmest ones (the highest temperatures are found in the heart, intestine and brain). On the contrary, the influence of field orientation and related eddy current effects is evident for the rat. In this case, the temperature peaks are mainly localized at the body surface, with an internal extension larger when the field is applied orthogonally to the animal longitudinal axis. The maximum temperature values are found in muscles, connective tissue and skin.

The time evolutions of the average and maximum temperature increases experienced by the two animals during the heating-cooling transients are reported in Fig. 5b. For the entire duration, the temperature increments

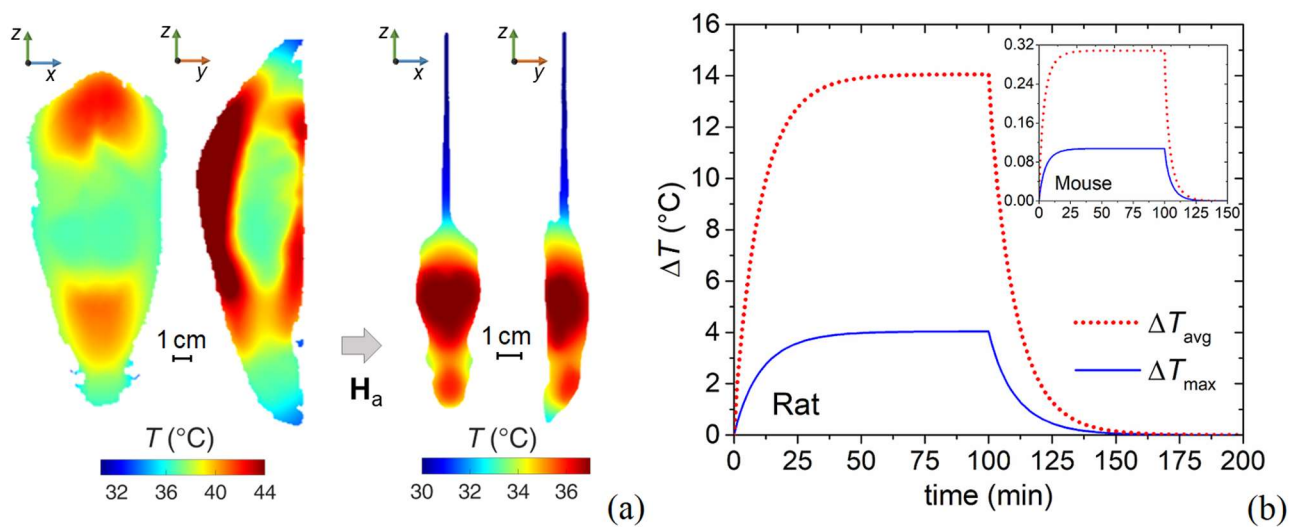


Fig. 5. (a) Maps of the temperature spatial distribution at thermal equilibrium calculated over two longitudinal sections of the 503 g rat (left) and 28 g mouse (right), when the AC magnetic field is applied uniformly and transversally to the body longitudinal axis with a peak amplitude of 50 kA/m and a frequency of 100 kHz. (b) Corresponding time evolutions of the average and maximum temperature increases during the heating-cooling transients; the data for the mouse are reported in the inset (with the same measure units of the main graph).

observed in both the mouse and rat correspond to almost twice the values estimated when the field is parallel to the body longitudinal axis.

4.4 Influence of heat transfer coefficient

The non-negligible increase in temperature found in rats, when exposed to EM fields even satisfying the Hergt-Dutz limit, can have a significant impact on their physiological conditions. As this effect is more intense on the body surface, a precaution to prevent excessive temperature increments on the skin is the use of water boluses [61,62]. Other mitigation solutions for local heating comprise the intermittent application of magnetic field (in an ON/OFF pulse mode) and the coil displacement [63,64].

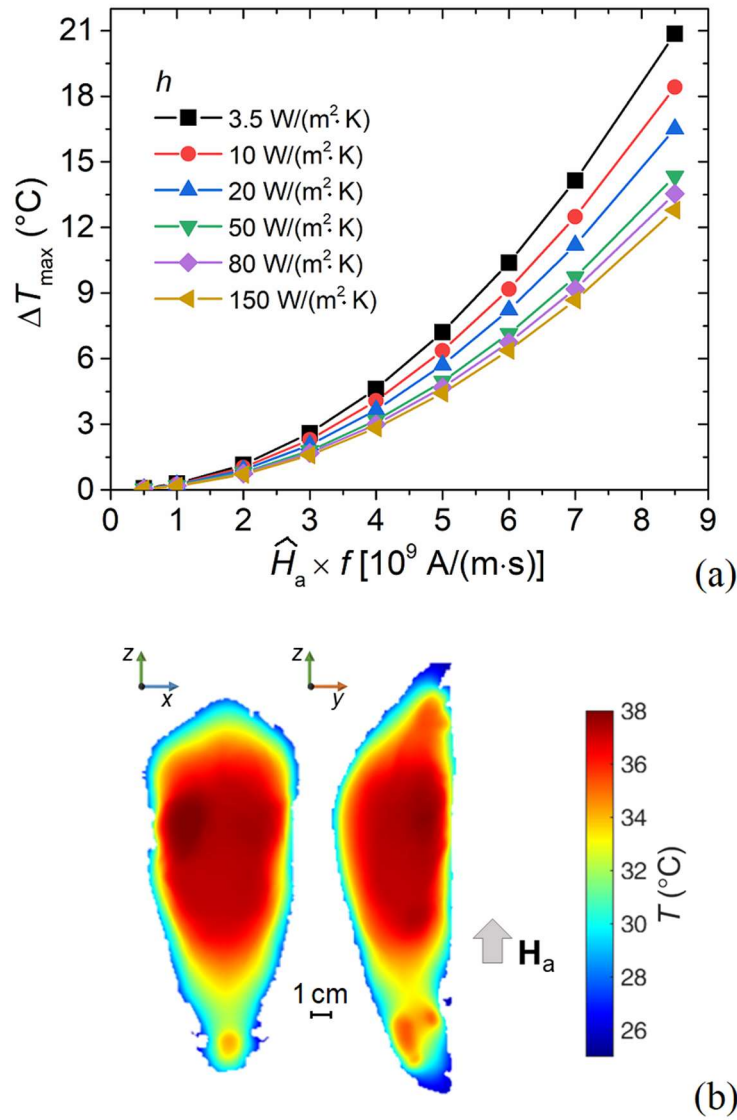


Fig. 6. (a) Influence of the heat transfer coefficient h on the maximum temperature increase estimated in the 503 g rat, versus the product of the AC magnetic field frequency and peak amplitude. The field is uniformly applied along the body longitudinal axis. (b) Maps of the temperature spatial distribution at thermal equilibrium calculated over two longitudinal sections of the rat, for $h = 80$ W/(m²·K) and $\hat{H}_a \times f = 5 \cdot 10^9$ A/(m·s).

The introduction of cooling systems like water boluses leads to a condition of forced convection at the interface between the skin and the external environment. This is associated with an increment of the outward heat flux, which can be described in (9) via an increase in the heat transfer coefficient h , which depends on the water bolus thickness and thermal conductivity of the bag material [61].

To simulate different cooling conditions under forced convection, we vary coefficient h within the range 3.5-150 W/(m²·K) [62], assuming that the water circulating inside the bolus has a constant temperature of 25 °C. As a first approximation, h is uniformly modified over the entire body surface. The maximum temperature increases found in the 503 g rat for the considered values of h and applying the field along the body longitudinal axis are reported in Fig. 6a, versus $\hat{H}_a \times f$. In comparison to the values obtained by setting h at 3.5 W/(m²·K), when $h = 150$ W/(m²·K) the maximum and average temperature increases reduce by 39% and 56%, respectively.

We can also observe that the temperature increments have an asymptotic behaviour versus h , since for very high values of h the eddy current effects are strongly mitigated and the thermal state tends to metabolic condition. This is well illustrated by Fig. 6b, which shows the temperature spatial distributions at thermal equilibrium, calculated over longitudinal sections of the rat for $h = 80$ W/(m²·K) and $\hat{H}_a \times f = 5 \cdot 10^9$ A/(m·s). The temperature peaks are no more concentrated on the peripheral tissues, as for the case of free convection (Fig. 4a), but internally.

4.5 Role of applicator geometry

In the previous analysis we assume that the entire body is exposed to a uniform magnetic field; this hypothesis can be considered valid for applicators based on helical coils, when the animal is placed totally within the coil. However, in many preclinical studies the AC magnetic field invests only a small portion of the body, since the coil does not surround the entire animal, but it is placed in close proximity to the target region (tumour to be treated). In this case, the treatment is done under safer conditions, enabling us to reduce the appearance of hot spots in healthy tissues.

To investigate the possible mitigation of eddy current effects consequent to a more localized EM field exposure, we consider two different applicators, namely an 8-turn helical coil and a pancake coil (both with an outer diameter of 5 cm). These are similar to geometrical configurations already used in preclinical tests on

murine models [36,37] and to available commercial applicators [33]. The two coils are positioned in closed proximity to the target region, which is a $2.4 \times 3.7 \times 3.8 \text{ cm}^3$ tumour placed on the rat right flank and with centre distant about 1 cm from the skin (see Fig. 7a). The coils are supplied with a current of 300 A and positioned in a way to guarantee that the magnetic field within the tumour is sufficiently large to enable the activation of standard MNPs, when a frequency of 300 kHz is considered [31].

Fig. 7b shows the maps of the magnetic field spatial distribution calculated on a plane that crosses the rat body and contains the tumour centre, as schematized in Fig. 7a. For the 8-turn helical coil, in the tumour region the field varies between 3.8 and 17.5 kA/m, with an average value of 8.5 kA/m. For the pancake coil, in the tumour region the field is characterized by a stronger gradient, varying between 2 and 28.2 kA/m, with an average value of 7.2 kA/m. In comparison to the case of uniform field, the large variation of the magnetic field amplitude within the target region can impact on the treatment efficacy, since the specific loss power of MNPs is a function of the field magnitude [31,32]. As an advantage, the corresponding values of SAR are strongly reduced, being the regions interested by eddy current effects localized in the only area exposed to the EM field. A whole-body average SAR of 0.3 W/kg is estimated for the 8-turn helical coil, while a value of 0.1 W/kg is obtained for the pancake coil.

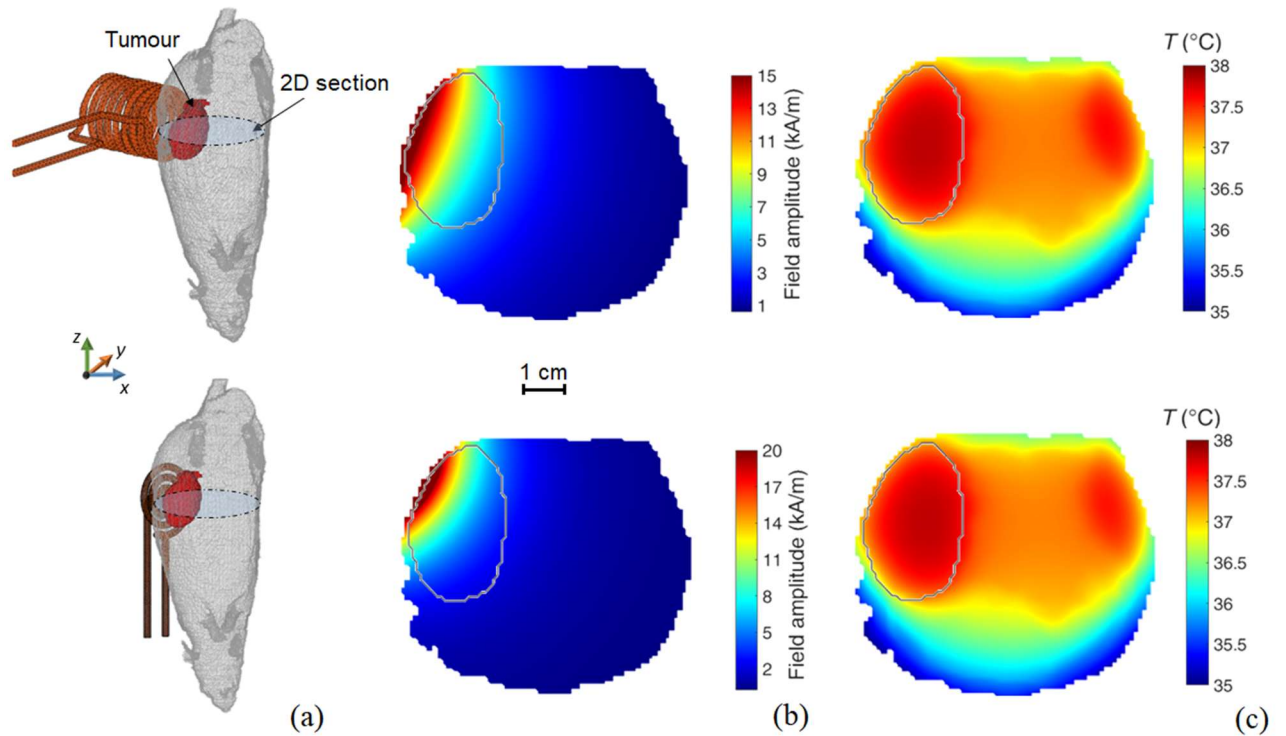


Fig. 7. (a) Schematics illustrating the position of the 8-turn coil (top) and pancake coil (bottom) with respect to the 503 g rat, with the target region (tumour) coloured in red. (b) Maps of the magnetic field amplitude, calculated over the rat transversal section, depicted in light blue in (a), for a supply current of 300 A. (c) Corresponding maps of the temperature spatial distribution at thermal equilibrium calculated over the same transversal section, when the frequency of the AC magnetic field is 300 kHz. The tumour boundary is indicated with a grey line.

From the thermal simulations, it results that the temperature spatial distribution is similar to the case when no field is applied, with the brain, heart, intestine and tumours as the warmest areas, due to metabolic heat dominance. The average temperature increase is in fact negligible. Also the highest temperature increments, which are concentrated on the muscle peripheral tissues, near to the coils, are very low, being 0.36 °C and 0.18 °C for the 8-turn helical coil and the pancake coil, respectively. The largest eddy current effects, despite very limited, are found for the former, due to the presence of more extended areas (going from the skin to the tumour centre), where the magnetic field amplitude is such that $\hat{H}_a \times f$ is close to the Hergt-Dutz limit.

If the portion of the body exposed to the EM field is relatively larger, the eddy current effects can be no more negligible also for the case of localized EM field exposure. As an example, if we resize the digital phantom of the rat to a length of 11.2 cm (excluding tail), we observe a maximum temperature increase of about 1.3 °C, when considering a 300 kHz magnetic field source with geometrical configuration, dimensions, supplied current and position similar to the case depicted in Fig. 7a. This result is in line with the experimental findings in [36], where a maximum temperature increase around 2 °C was obtained in a comparable murine model, exposed to a 300 kHz magnetic field generated by a coil with features similar to the case above. The slight discrepancies can originate from a non-perfect reproduction, with simulations, of the experimental test in terms of coil geometry, size and location with respect to the body, as well as from differences in murine model anatomy, tissue electrical and thermal properties, and type of heat exchange with the surrounding environment.

5. Conclusions

In this study, we have investigated by means of *in silico* simulations the possible occurrence of non-negligible eddy current effects during preclinical tests of magnetic hyperthermia. In particular, we have demonstrated that for animals of very small size, like mice weighting less than 30 g, the thermal effects induced by AC magnetic fields are very modest, also when slightly overcoming the Hergt-Dutz limit. Important effects can be observed only for very large values of the product $\hat{H}_a \times f$. As an example, when $\hat{H}_a = 40$ kA/m and $f = 500$ kHz, a maximum temperature increase higher than 2 °C is found on the skin.

As shown in our study, eddy current effects are no more negligible in animals with larger size, like rats. In particular, we have observed that in 500 g rats exposed to a uniform magnetic field along the body longitudinal

axis, maximum temperature increases lower than 1 °C are found only when $\hat{H}_a \times f$ does not exceed the value of $2 \cdot 10^9$ A/(m·s). Higher temperature increments are observed when the field is applied transversally, due to the enlargement of the body section orthogonal to the field.

The obtained results demonstrate that the Hergt-Dutz limit could not be considered as a condition that guarantees a safe level of EM field exposure for animals with size comparable to rats or larger, with obvious consequences on its validity in human applications. Anyway, a strong mitigation of eddy current effects can be obtained when introducing water boluses, due to the forced heat convection at the interface between the skin and the surrounding environment. Another strategy to reduce eddy current effects is a partial exposure of the body to the AC magnetic fields, thanks to a proper selection of the applicator geometry and positioning with respect to the target region. We have observed that with helical or pancake coils placed in proximity to the tumour, a strong decay of SAR can be obtained, with negligible temperature increases in the superficial tissues closer to the coils. Conversely, the achievement of high level of magnetic field uniformity becomes very critical within extended tumours, due to the presence of elevated gradients.

Finally, the physics-based numerical modelling approach here developed can be used as a predictive tool to guide and optimize *in vivo* tests of magnetic hyperthermia. In this specific case, it can be employed to select the magnetic field parameters and treatment conditions to avoid the appearance of hot spots in healthy regions.

Acknowledgments

This work was supported by Project 18HLT06 RaCHy, which has received funding from the European Metrology Programme for Innovation and Research (EMPIR), co-financed by the participating states, and from the European Union's Horizon 2020 Programme.

Declaration of competing interests

None to be declared.

References

- [1] H. P. Kok *et al.*, “Heating technology for malignant tumors: a review”, *Int. J. Hyperthermia*, vol. 37, no. 1, pp. 711-741, 2020.
- [2] N. R. Datta *et al.*, “Local hyperthermia combined with radiotherapy and/or chemotherapy: Recent advances and promises for the future”, *Cancer Treatment Reviews*, vol. 41, no. 9, pp. 742-753, 2015.
- [3] J. van der Zee, “Heating the patient: a promising approach?”, *Annals of Oncology*, vol. 13, no. 8, pp. 1173-1184, 2002.
- [4] S. Jha, P. K. Sharma, and R. Malviya, “Hyperthermia: Role and risk factor for cancer treatment”, *Achievements in the Life Sciences*, vol. 10, no. 2, pp. 161-167, 2016.
- [5] B. Kozissnik, A. C. Bohorquez, J. Dobson, and C. Rinaldi, “Magnetic fluid hyperthermia: Advances, challenges, and opportunity”, *Int. J. Hyperthermia*, vol. 29, no. 8, pp. 706–714, 2013.
- [6] M. Bañobre-López, A. Teijeiro, and J. Rivas, “Magnetic nanoparticle-based hyperthermia for cancer treatment”, *Reports of Practical Oncology & Radiotherapy*, vol. 18, no. 6, pp. 397-400, 2013.
- [7] E. A. Périgo *et al.*, “Fundamentals and advances in magnetic hyperthermia”, *Appl. Phys. Rev.*, vol. 2, no. 4, 2015, Art. No. 041302.
- [8] X. Liu *et al.*, “Comprehensive understanding of magnetic hyperthermia for improving antitumor therapeutic efficacy”, *Theranostics*, vol. 10, no. 8, pp. 3793–3815, 2020.
- [9] Q. A. Pankhurst, J. Connolly, S. K. Jones, and J. Dobson, “Applications of magnetic nanoparticles in biomedicine”, *J. Phys. D: Appl. Phys.*, vol. 36, pp. R167–R181, 2003.
- [10] A.-R. Tsiapla *et al.*, “Mitigation of magnetic particle hyperthermia side effects by magnetic field controls”, *Int. J. Hyperthermia*, vol. 38, no. 1, pp. 511-522, 2021.
- [11] W. J. Atkinson, I. A. Brezovich, and D. P. Chakraborty, “Usable frequencies in hyperthermia with thermal seeds”, *IEEE Transactions on Biomedical Engineering*, vol. BME-31, no. 1, pp. 70-75, 1984.
- [12] R. Hergt, and S. Dutz, “Magnetic particle hyperthermia - biophysical limitations of a visionary tumour therapy”, *J. Magn. Magn. Mater.*, vol. 311, no. 1, pp. 187-192, 2007.
- [13] S. Kossatz *et al.*, “Efficient treatment of breast cancer xenografts with multifunctionalized iron oxide nanoparticles combining magnetic hyperthermia and anti-cancer drug delivery”, *Breast Cancer Research*, 17:66, 2015. DOI: 10.1186/s13058-015-0576-1.
- [14] S. Pichler *et al.*, “Iron oxide nanoparticles as carriers for DOX and magnetic hyperthermia after intratumoral application into breast cancer in mice: Impact and future perspectives”, *Nanomaterials*, vol. 10, no. 6, 2020, Art. No. 1016.
- [15] A. Espinosa *et al.*, “Magnetic (hyper)thermia or photothermia? Progressive comparison of iron oxide and gold nanoparticles heating in water, in cells, and in vivo”, *Adv. Funct. Mater.*, vol. 28, no. 37, 2018, Art. No. 1803660.
- [16] A. P. Sangnier *et al.*, “Targeted thermal therapy with genetically engineered magnetite magnetosomes@RGD: Photothermia is far more efficient than magnetic hyperthermia”, *Journal of Controlled Release*, vol. 279, pp. 271–281, 2018.
- [17] A. Curcio *et al.*, “Iron oxide nanoflowers@CuS hybrids for cancer tri-therapy: Interplay of photothermal therapy, magnetic hyperthermia and photodynamic therapy”, *Theranostics*, vol. 9, no. 5, pp. 1288-1302, 2019.
- [18] Z.-Q. Zhang, and S.-C. Song, “Thermosensitive/superparamagnetic iron oxide nanoparticle-loaded nanocapsule hydrogels for multiple cancer hyperthermia”, *Biomaterials*, vol. 106, pp. 13-23, 2016.
- [19] O. Sandre *et al.*, “In vivo imaging of local gene expression induced by magnetic hyperthermia”, *Genes*, vol. 8, no. 2, 2017, Art. No. 61.

- [20] N. A. Brusentsov *et al.*, “Magnetic fluid hyperthermia of the mouse experimental tumor”, *J. Magn. Magn. Mater.*, vol. 252, pp. 378-380, 2002.
- [21] C. L. Dennis *et al.*, “Nearly complete regression of tumors via collective behavior of magnetic nanoparticles in hyperthermia”, *Nanotechnology*, vol. 20, no. 39, 2009, Art. No. 395103.
- [22] X. Ma *et al.*, “Fe₃O₄-Pd Janus nanoparticles with amplified dual-mode hyperthermia and enhanced ROS generation for breast cancer treatment”, *Nanoscale Horizons*, vol. 4, pp. 1450-1459, 2019.
- [23] H. A. Albarqi *et al.*, “Systemically delivered magnetic hyperthermia for prostate cancer treatment”, *Pharmaceutics*, vol. 12, no. 11, 2020, Art. No. 1020.
- [24] X. L. Liu *et al.*, “Synthesis of ferromagnetic Fe_{0.6}Mn_{0.4}O nanoflowers as a new class of magnetic theranostic platform for in vivo T₁-T₂ dual-mode magnetic resonance imaging and magnetic hyperthermia therapy”, *Adv. Healthcare Mater.*, vol. 5, no. 16, pp. 2092-2104, 2016.
- [25] J. Lee *et al.*, “Exchange-coupled magnetic nanoparticles for efficient heat induction”, *Nature Nanotechnology*, vol. 6, pp. 418-422, 2011.
- [26] O. K. Arriortua *et al.*, “Antitumor magnetic hyperthermia induced by RGD-functionalized Fe₃O₄ nanoparticles, in an experimental model of colorectal liver metastases”, *Beilstein J. Nanotechnol.*, vol. 7, pp. 1532-1542, 2016.
- [27] L. Beola, L. Gutiérrez, V. Grazú, and L. Asín, “A roadmap to the standardization of in vivo magnetic hyperthermia”, in *Nanomaterials for Magnetic and Optical Hyperthermia Applications*, Elsevier, 2019, ch. 12, sec. C, pp. 317-337.
- [Online]. Available: <https://www.sciencedirect.com/book/9780128139288>.
- [28] H. F. Rodrigues, G. Capistrano, and A. F. Bakuzis, “In vivo magnetic nanoparticle hyperthermia: a review on preclinical studies, low-field nano-heaters, noninvasive thermometry and computer simulations for treatment planning”, *Int. J. Hyperthermia*, vol. 37, no. 3, 76-99, 2020.
- [29] International Commission on Non-Ionizing Radiation Protection (ICNIRP), “Guidelines for limiting exposure to time-varying electric and magnetic fields (1 Hz to 100 kHz)”, *Health Phys.*, vol. 99, no. 6, pp. 818-836, 2010.
- [30] J. M. Osepchuk, and R. C. Petersen, “Historical review of RF exposure standards and the International Committee on Electromagnetic Safety (ICES)”, *Bioelectromagnetics Supplement*, vol. 6, pp. S7-S16, 2003.
- [31] F. Soetaert, S. K. Kandala, A. Bakuzis, and R. Ivkov, “Experimental estimation and analysis of variance of the measured loss power of magnetic nanoparticles”, *Scientific Reports*, vol. 7, 2017, Art. No. 6661.
- [32] R. Ferrero *et al.*, “Experimental and modelling analysis of the hyperthermia properties of iron oxide nanocubes”, *Nanomaterials*, vol. 11, no. 9, 2021, Art. No. 2179.
- [33] <https://www.nbnanoscale.com/coils-magnetic-hyperthermia/>.
- [34] M. Ohtake *et al.*, “Hyperthermia and chemotherapy using Fe(Salen) nanoparticles might impact glioblastoma treatment”, *Scientific Reports*, vol. 7, 2017, Art. No. 42783.
- [35] H. F. Rodrigues *et al.*, “Precise determination of the heat delivery during *in vivo* magnetic nanoparticle hyperthermia with infrared thermography”, *Phys. Med. Biol.*, vol. 62, pp. 4062-4082, 2017.
- [36] H. F. Rodrigues *et al.*, “Real-time infrared thermography detection of magnetic nanoparticle hyperthermia in a murine model under a non-uniform field configuration”, *Int. J. Hyperthermia*, vol. 29, pp. 752-767, 2013.
- [37] T. Araya *et al.*, “Antitumor effects of inductive hyperthermia using magnetic ferucarbotran nanoparticles on human lung cancer xenografts in nude mice”, *Onco Targets Ther.*, vol. 6, pp. 237-242, 2013.
- [38] R. Scorretti, N. Burais, O. Fabregue, A. Nicolas, and L. Nicolas, “Computation of the induced current density into the human body due to relative LF magnetic field generated by realistic devices”, *IEEE Trans. Magn.*, vol. 40, no. 2, pp. 643-646, 2004.

- [39] H. Corte-León *et al.*, “Comparison and validation of different magnetic force microscopy calibration schemes”, *Small*, vol. 16, no. 11, 2020, Art. No. 1906144.
- [40] A. González-Suárez, J. J. Pérez, R. M. Irastorza, A. D'Avila, and E. Berjano, “Computer modeling of radiofrequency cardiac ablation: 30 years of bioengineering research”, *Computer Methods and Programs in Biomedicine*, 106546, Available online 18 November 2021 (in press).
- [41] A. Attaluri *et al.* “Magnetic nanoparticle hyperthermia enhances radiation therapy: A study in mouse models of human prostate cancer”, *Int. J. Hyperthermia*, vol. 31, no. 4, pp. 359-374, 2015.
- [42] A. Manzin, R. Ferrero, and M. Vicentini, “From micromagnetic to *in silico* modelling of magnetic nanodisks for hyperthermia applications”, *Adv. Theory Simul.*, vol. 4, no. 5, 2021, Art. No. 2100013.
- [43] I. Laakso, and A. Hirata, “Dominant factors affecting temperature rise in simulations of human thermoregulation during RF exposure”, *Phys. Med. Biol.*, vol. 56, no. 23, pp. 7449-7471, 2011.
- [44] <https://zmt.swiss/sim4life/>.
- [45] <https://itis.swiss/virtual-population/animal-models/animals/>.
- [46] B. Dogdas, D. Stout, A. F. Chatziioannou, and R. M. Leahy, “Digimouse: a 3D whole body mouse atlas from CT and cryosection data”, *Physics in Medicine & Biology*, vol. 52, no. 3, 2007, Art. No. 577.
- [47] <https://itis.swiss/virtual-population/tissue-properties/overview/>.
- [48] A. Trakic, F. Liu, and S. Crozier, “Transient temperature rise in a mouse due to low-frequency regional hyperthermia”, *Phys. Med. Biol.*, vol. 51, no. 7, pp. 1673-1691, 2006.
- [49] L. Bubnovskaya *et al.*, “Magnetic fluid hyperthermia of rodent tumors using manganese perovskite nanoparticles”, *Journal of Nanoparticles*, vol. 2014, 2014, Art. No. 278761.
- [50] M. Johannsen *et al.*, “Magnetic fluid hyperthermia (MFH) reduces prostate cancer growth in the orthotopic Dunning R3327 rat model”, *Prostate*, vol. 64, no. 3, pp. 283-292, 2005.
- [51] F. Oltolina *et al.*, “Biomimetic magnetite nanoparticles as targeted drug nanocarriers and mediators of hyperthermia in an experimental cancer model”, *Cancers*, vol. 12, no. 9, 2020, Art. No. 2564.
- [52] T. J. Carter *et al.*, “Potential of magnetic hyperthermia to stimulate localized immune activation”, *Small*, vol. 17, no. 14, 2021, Art. No. e2005241.
- [53] W. Lin *et al.* “Thermosensitive magnetic liposomes with doxorubicin cell-penetrating peptides conjugate for enhanced and targeted cancer therapy”, *Drug Delivery*, vol. 23, no. 9, pp. 3436-3443, 2016.
- [54] G. Capistrano *et al.*, “Noninvasive intratumoral thermal dose determination during *in vivo* magnetic nanoparticle hyperthermia: combining surface temperature measurements and computer simulations”, *Int. J. Hyperthermia*, vol. 37, no. 1, pp. 711–741, 2020.
- [55] Y. Gong, M. H. Capstick, S. Kuehn, P. F. Wilson, J. M. Ladbury, G. Koepke, D. L. McCormick, R. L. Melnick, and N. Kuster, “Life-Time Dosimetric Assessment for Mice and Rats Exposed in Reverberation Chambers for the Two-Year NTP Cancer Bioassay Study on Cell Phone Radiation”, *IEEE Trans. Electromagn. Compat.*, vol. 59, no. 6, pp. 1798-1808, 2017.
- [56] X. L. Liu *et al.*, “Magnetic vortex nanorings: A new class of hyperthermia agent for highly efficient *in vivo* regression of tumors”, *Adv. Mater.*, vol. 27, no. 11, pp. 1939-1944, 2015.
- [57] R. Ferrero *et al.*, “Influence of shape, size and magnetostatic interactions on the hyperthermia properties of permalloy nanostructures”, *Scientific Reports*, vol. 9, 2019, Art. No. 6591.

- [58] S. Kodera, J. Gomez-Tames, A. Hirata, H. Masuda, T. Arima, and S. Watanabe, “Multiphysics and Thermal Response Models to Improve Accuracy of Local Temperature Estimation in Rat Cortex under Microwave Exposure”, *Int. J. Environ. Res. Public Health*, vol. 14, no. 4, 2017, Art. No. 358.
- [59] A. Hirata, S. Watanabe, M. Kojima, I. Hata, K. Wake, M. Taki, K. Sasaki, O. Fujiwara, and T. Shiozawa, “Computational Verification of Anesthesia Effect on Temperature Variations in Rabbit Eyes Exposed to 2.45 GHz Microwave Energy”, *Bioelectromagnetics*, vol. 27, no. 8, pp. 602-612, 2006.
- [60] S.-W. Ding *et al.*, “Magnetic hydrogel with long in situ retention time for self-regulating temperature hyperthermia”, *Int. J. Hyperthermia*, vol. 38, no. 1, pp. 13-21, 2021.
- [61] A. Bakker *et al.*, “Clinical feasibility of a high-resolution thermal monitoring sheet for superficial hyperthermia in breast cancer patients”, *Cancers*, vol. 12, no. 12, 2020, Art. No. 3644.
- [62] M. L. Van Der Gaag, M. De Bruijne, T. Samaras, J. Van Der Zee, and G. C. Van Rhoon, “Development of a guideline for the water bolus temperature in superficial hyperthermia”, *Int. J. Hyperthermia*, vol. 22, no. 8, pp. 637-656, 2006.
- [63] G. Pefanis, N. Maniotis, A.-R. Tsiapla, A. Makridis, T. Samaras, and M. Angelakeris, “Numerical Simulation of Temperature Variations during the Application of Safety Protocols in Magnetic Particle Hyperthermia”, *Nanomaterials*, vol. 12, no. 3, 2022, Art. No. 554.
- [64] A. Balousis, N. Maniotis, and T. Samaras, “Improvement of Magnetic Particle Hyperthermia: Healthy Tissues Sparing by Reduction in Eddy Currents”, *Nanomaterials*, vol. 11, no. 2, 2021, Art. No. 556.